Earth and Planetary Science Letters 547 (2020) 116426

Contents lists available at ScienceDirect

Earth and Planetary Science Letters

www.elsevier.com/locate/epsl

On the eruptive origins of lunar localized pyroclastic deposits

Amber L. Keske *, Amanda B. Clarke, Mark S. Robinson

School of Earth and Space Exploration, Arizona State University, P.O. Box 876004, Tempe, AZ 85287-6004, United States of America

ARTICLE INFO

Article history:
Received 28 October 2018
Received in revised form 21 February 2020
Accepted 16 June 2020
Available online xxxx
Editor: W.B. McKinnon

Keywords:
volcanism
Moon
basaltic volcanism
explosive volcanism
Moon, surface
lunar volatiles

ABSTRACT

Localized pyroclastic deposits (LPDs) are low-albedo accumulates of pyroclastic material with distinct positive topographic signatures that are found dominantly along highland-mare boundaries. Previous workers hypothesized that LPDs represent products of a lunar equivalent of Vulcanian-style eruptions, based in part on the observation that some of the deposits in Alphonsus Crater have large vent volumes in comparison with their deposit volumes, indicating a low proportion of juvenile material in the deposits. The objective of this study is to better understand eruption mechanisms by determining how the proportion of juvenile material, as calculated using deposit and vent volumes, varies among LPDs in Alphonsus Crater and elsewhere on the Moon using contemporary data and methods. Deposit and vent volumes for 23 LPDs from eleven sites were calculated by differencing current and modeled pre-eruption surfaces using digital terrain models (DTMs) derived from Lunar Reconnaissance Orbiter Camera Narrow Angle Camera (LROC NAC). Results show that LPDs have a wide range of juvenile proportions, many of which are more juvenile-rich than previously thought. Additionally, there is a positive relationship between juvenile material proportion and deposit volume and thickness, and a positive relationship between juvenile volume and dispersal area. LPDs also bear a broad range of thinning profiles which span a range of multiple eruption types on Earth. These findings, along with previous studies employing spectroscopic analysis of these deposits, indicate there is greater diversity among LPDs in composition and morphometry than previously understood, and that previously published simplified Vulcanian models may apply only to the deposits containing the least amount of juvenile material, with all others perhaps requiring a combination of multiple eruptive mechanisms. Furthermore, dynamic model results suggest that the most widespread lunar deposits in this study were formed by magma containing 2000–5000 ppm of dissolved volatiles, consistent with recent estimates via melt inclusion analysis, but contrary to long-held ideas that the Moon was largely degassed during its formation.

1. Introduction

Lunar dark mantle deposits (DMDs) are low-albedo, friable material dominantly found along highland-mare boundaries and are thought to be pyroclastic in origin (e.g., Carr, 1996; Schmitt et al., 1967; Wilhelms and McCauley, 1971; El-Baz, 1972; Sato, 1976). Although pyroclastic deposits represent a volumetrically negligible proportion of all volcanic material on the Moon, they may include some of its most primitive and volatile-rich components (Gaddis et al., 1985), and therefore are crucial for understanding lunar basaltic magmatism. Additionally, the high FeO content of these pyroclastic glasses has led to increased interest in their potential as a source of oxygen in future exploration endeavors (Allen, 2015). Previous workers (e.g., Head and Wilson, 1979; Gaddis et al., 1985) divided lunar pyroclastic deposits into two groups: "regional" dark mantle deposits (RDMDs), characterized by thin, flat blanketing deposits covering areas on the order of thousands of square kilometers, and "localized" dark mantle deposits (LDMDs), which are smaller (typically less than 100 km^2 in areal extent) with a resolvable positive topographic signature.

The eruption mechanisms responsible for differences in RDMDs and LDMDs were evaluated by Head and Wilson (1979), who characterized both deposit types using photogrammetrically-derived topography from Apollo 16 Panoramic Camera images. The authors then compared their observations to models of expected morphology resulting from various eruption types that may operate on the lunar surface. They proposed that wide dispersal of pyroclastic material characteristic of RDMDs is likely the result of the lunar equivalent of Strombolian-type activity (i.e., coalesced bubble explosions), while the proximal accumulation of coarse clasts and limited dispersal of fine ash particulates more closely resembles deposits resulting from Vulcanian-type eruptions involving explosive fragmentation of a solid, near-surface plug composed of wall

* Corresponding author.
E-mail address: alkeske@asu.edu (A.L. Keske).

https://doi.org/10.1016/j.epsl.2020.116426
0012-821X/

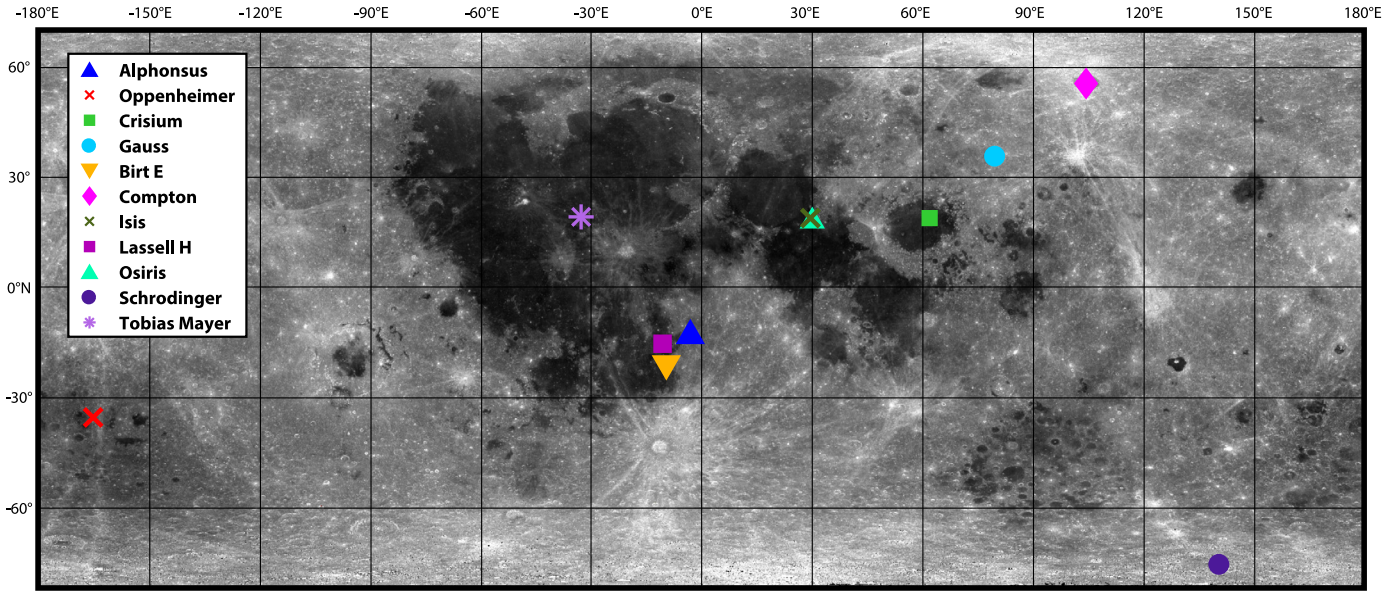

Fig. 1. Locations of the eleven LPD sites included in this study on a global 643 nm WAC mosaic (Boyd et al., 2013). (For interpretation of the colors in the figure(s), the reader is referred to the web version of this article.)

rock material. The latter conclusion also relied heavily on the results of their volumetric measurements of six deposits and their vents in Alphonsus Crater, which indicated little or no juvenile component to the deposits, despite the low-albedo of the deposits compared to the surrounding crater floor. In particular, Alphonsus 1 (also known as Ravi) was calculated to have the smallest proportion of juvenile material, and was thus cited as the strongest indicator that LDMD deposits are composed chiefly of bedrock material (i.e., non-juvenile magma), and that the eruption mechanism producing LDMDs must involve significant fracturing and entrainment of wall rock material. This hypothesis influenced later interpretations of compositional groups of pyroclastic deposits that were categorized using spectra collected both telescopically (e.g., Gaddis et al., 1985; Hawke et al., 1985, 1989) and with the five-band Clementine ultraviolet-visible (UVVIS) instrument (Nozette, 1995) (e.g., Gaddis et al., 2000, 2003). It is therefore important to verify that the morphometric relationships described by Head and Wilson (1979) hold true for the Alphonsus deposits, given more contemporary data and methods, as well as for other LDMDs to confirm that their hypothesis indeed applies to all LDMDs. Later works revised RDMDs as being Hawaiian-type in origin, and instead categorized cones (which are similar to LDMDs but with somewhat steeper slopes) as being Strombolian in origin (Head and Wilson, 2017).

Although the notion that LDMDs are products of lunar Vulcanian-like eruptions is generally accepted (e.g., Gaddis et al., 2003; Gustafson et al., 2012), the physical details of such events remain poorly constrained due to uncertainties related to the extent to which juvenile magma participates in the eruption and affects LDMD spectral reflectance in visible and near-infrared wavelengths. In order to better understand the nature of LDMD magma parent bodies and lunar mantle volatile content and composition using spectral reflection measurements, improved estimates of the volume of juvenile vs. bedrock material in LDMDs are necessary. The objective of this study is to determine how the relative proportions of bedrock and juvenile material vary in LDMDs as indicated by their deposit-to-vent-volume ratio, how the results compare with interpretations of deposit composition using remote sensing-based reflection spectra, and what the implications may be for lunar eruption mechanisms. Because the distinction between LDMDs and cones is poorly defined, cones are included in this study as well. Henceforth, the deposits in this study are collectively referred to as localized pyroclastic deposits (LPDs).

2. Methods

2.1. Volume estimates

The morphology of 23 LPD deposits from eleven sites across the Moon (Fig. 1) were investigated with the specific goal of quantifying the amount of juvenile material in each deposit using the difference between the exterior tephra deposit volume and vent volume. Sixteen of the deposits are found in floor-fractured craters (Jozwiak et al., 2015): Alphonsus crater, Oppenheimer crater, Gauss crater, Compton crater, and Schrödinger crater. Seven of the deposits are found at six sites located within mare: northeast Crisium, Birt, Isis, Lassell H, Osiris, and Tobias Mayer. These 23 sites were selected based on the topographic simplicity of the surroundings and the deposits themselves, the presence of a (preferably singular) central vent, and the availability of stereo images from the Lunar Reconnaissance Orbiter Camera (LROC) Narrow Angle Camera (NAC) (Robinson et al., 2010) for the production of high-resolution (~3–5 m horizontal pixel scale) Digital Terrain Models (DTMs) using SOCET SET (Henriksen et al., 2017). Since the vent slopes are steep (>20°), small uncertainties in slope can dramatically change the vent volume estimates. Where gaps in NAC DTM coverage on the surrounding LPD deposit exist, they were filled using data from the 60°S to 60°N 512 PPD Lunar Orbiter Laser Altimeter (LOLA) (Smith et al., 2010) and SELENE Terrain Camera merge (Haruyama et al., 2014; Barker et al., 2016). Since this product does not cover Schrödinger Crater, gaps at that location were instead filled using the LOLA global DTM.

To determine the volume of each deposit, a corresponding DTM of an estimated pre-depositional surface was synthesized based on the pre-existing topography exposed around the deposit, profiles across the deposit, and exposed stratigraphy as seen in NAC images. Deposit boundaries were determined from reflectance and FeO contrasts with the surrounding terrain from a 100 m pixel scale photometrically normalized map produced from observations at 643 nm by the LROC Wide Angle Camera (WAC) (Boyd et al., 2013) and the global Clementine UVVIS iron abundance map (Lucey et al., 1995), respectively. The boundaries were checked

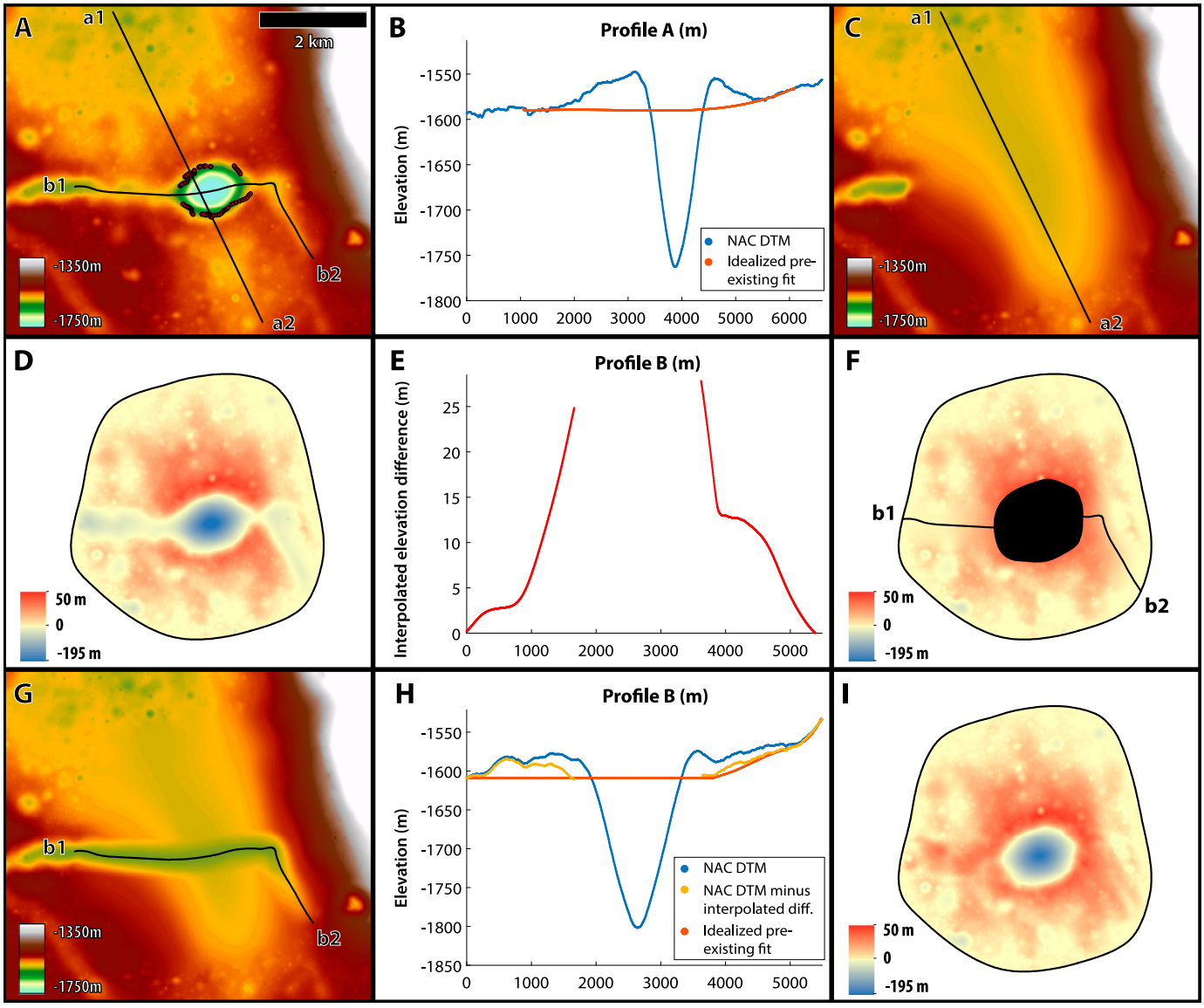

Fig. 2. Example of pre-existing surface derivation at Alphonsus 2 using NAC DTM profiles. A representative topographic profile a1–a2 (shown in panel A) was used to produce a model profile of the pre-existing surface without the rille (panel B). That profile is then used to interpolate a 3D surface (panel C). That surface is then subtracted from the NAC DTM (panel D), the rille removed, and the missing area interpolated to produce a new difference (or thickness) DTM (panel F, thickness profile along rille shown in panel E). The thickness profile extracted from the interpolated difference DTM is then subtracted from the NAC DTM and used to produce a best-guess model profile of the rille floor (panel H). That profile is then incorporated into a new 3D model of the pre-existing surface including the rille (panel G, final difference (i.e., thickness) DTM shown in panel I).

with low-incidence angle NAC images where available. The pyroclastic unit was then masked from the DTM and a new surface was generated using the ArcMap Spline tool (ESRI, 2011), which generates a minimum curvature surface. This method allowed us to use the surrounding topography for extrapolating the simplest underlying surface possible. This tool was also used to model underlying rilles and fractures, which are assumed to have existed prior to deposit emplacement. Since rille topography tends to be more irregular than inter-rille topography, in most cases one or a combination of three strategies for extrapolating the rille topography was employed: (1) using a simple linear model connecting the rille on one side of the deposit to the other, (2) applying the slope of the extrapolated topography outside of (and parallel to) the rille to the bottom of the rille, or (3) using representative profiles to determine a deposit thickness profile outside of the rille, and then subtracting that thickness profile from the present rille topography (Fig. 2).

Once a model of the pre-existing surface was produced (Fig. 2g), it was then subtracted from the present-day NAC DTM (Fig. 2a) containing the deposit, resulting in a surface difference DTM (Fig. 2i). In the difference DTM, positive values (shown in red) indicate deposit thickness and negative values (shown in blue) are vent depth values. The difference DTM guided the choice of rille extrapolation strategy, as it is expected that the thickness of the deposit smoothly decreases radially outward from the vent rim. The vent volume is the volume calculated by integrating the negative values of the difference DTM in the vent area, and the deposit volume is calculated by integrating the positive values of the entire difference DTM. This method allows for minimization of uncertainties resulting from complicated underlying topography, such as slopes, rilles, and/or scarps. Minimization of these uncertainties is of particular importance given the low-lying, low-relief nature of LPDs, and produces more realistic surface difference DTMs than when a simple flat plane is used.

For the purposes of this study, bedrock is defined to be the floor material (country rock) onto which the deposit was emplaced. Since the deposit contains a mix of juvenile tephra as well as the fragmented bedrock that was excavated to create the vent, the mass of juvenile material is:

$$m_{juvenile} = m_{deposit} - m_{excavated} \quad (1)$$

$$m_{juvenile} = \rho_{deposit} V_{deposit} - \rho_{bedrock} V_{vent} \quad (2)$$

where $V_{deposit}$ and V_{vent} are the estimated volumes of the deposit and the vent cavity, respectively, $\rho_{deposit}$ is the bulk density of the deposited material, and $\rho_{bedrock}$ is the bulk density of the bedrock prior to fragmentation and excavation. Assuming that the tephra sourced from bedrock material has the same bulk density as the tephra material sourced from juvenile magma (i.e., $\rho_{deposit} = \rho_{juvenile}$), the bulk volume of the juvenile component of the deposit can be obtained like so:

$$V_{juvenile} = \frac{m_{juvenile}}{\rho_{deposit}} \quad (3)$$

$$V_{juvenile} = \frac{\rho_{deposit} V_{deposit} - \rho_{bedrock} V_{vent}}{\rho_{deposit}} \quad (4)$$

$$V_{juvenile} = V_{deposit} - \frac{\rho_{bedrock} V_{vent}}{\rho_{deposit}} \quad (5)$$

In the absence of magmatic composition data, the dense-rock-equivalent (i.e., dense-magma-equivalent) volume cannot be calculated. We can instead calculate the bedrock-equivalent (BRE) volume:

$$V_{juvenile,BRE} = \frac{m_{juvenile}}{\rho_{bedrock}} \quad (6)$$

$$V_{juvenile,BRE} = \frac{\rho_{deposit} V_{deposit} - \rho_{bedrock} V_{vent}}{\rho_{bedrock}} \quad (7)$$

$$V_{juvenile,BRE} = V_{deposit} \frac{\rho_{deposit}}{\rho_{bedrock}} - V_{vent} \quad (8)$$

The deposit volume can then be used to determine the proportion of juvenile material in the deposit:

$$\%juvenile = 100 * \frac{V_{juvenile}}{V_{deposit}} \quad (9)$$

This modification of the calculation presented by Head and Wilson (1979) accounts for the change in bulk density of excavated vent material upon fragmentation during eruption, which was not considered by the previous authors. The range of values used for $\rho_{bedrock}$ varied by deposit location. For deposits located in floor-fractured craters, the density of pure anorthite was used as a dense endmember (2.7 g/cm^3), along with the bulk density range of lunar impact breccias reported by Kiefer et al. (2012), 2.3–2.6 g/cm^3. For deposits situated on mare, 3.0–3.3 g/cm^3 (Kiefer et al., 2012) was used, the upper end of which is extreme. For $\rho_{deposit}$, the bulk density of a sampled deposit of orange beads from Taurus-Littrow as measured by Gold et al. (1976) was reported as 1.4 g/cm^3. To account for potential variation in this value among deposit sites, we used this value with an uncertainty range of $\pm$0.1 g/cm^3. This uncertainty value reflects the variation of bulk densities measured for terrestrial basaltic tephra, which span $\sim$0.7–0.9 g/cm^3 (e.g., Costantini et al., 2009; Alfano et al., 2019); the lower terrestrial tephra densities are due to the fact that they are typically coarser and are made of up vesiculated scoria. The use of a range also alleviates artificial constraint of the solid volume fractions among all deposits, which would be inappropriate. Note that if one assumes a constant solid volume fraction among deposits, the density contrast range of orange beads with the mare bedrock (i.e., $\rho_{deposit}/\rho_{bedrock}$) could be applied for all settings, which would decrease absolute juvenile estimates for floor-fractured crater settings by less than 1% juvenile for deposits with the highest percentages of juvenile material to 20% juvenile for the lowest. When the volume of the vent exceeds the volume of the deposit, the expression returns a negative value, indicating negligible volume of juvenile material in the deposit.

2.2. Sources of uncertainty

Reported errors in juvenile percentages include bedrock density and DTM uncertainties. The uncertainty of NAC DTMs is given by the relative linear error value as calculated by SOCET SET, which uses the image ground sampling distance, convergence angle, and image matching uncertainty of the model to derive a vertical uncertainty for each DTM (typically less than 5 m) (Henriksen et al., 2017). The global LROC-SELENE DTM that was used for gaps in the NAC DTMS has a vertical accuracy of 3–4 m (Barker et al., 2016). Volumetric uncertainties were derived by multiplying the vertical uncertainty of the NAC DTM by area of the deposit it covers, and then adding to that value the area of any gaps multiplied by 4 m.

There are several errors that are not accounted for in the uncertainty calculations and are not represented by the error bars in subsequent plots due to insufficient data for quantifying their impact. For example, fallback of material into the vent during and after eruption would serve to exaggerate juvenile estimates, though evidently to a very minor degree (see section 2.3). Any post-eruptive subsidence resulting from evacuation of the magmatic plumbing system would also influence volumes in unpredictable ways. Another influence on the presented estimates is the accuracy of the estimated pre-existing surfaces. Examples of particularly complex sites from this dataset include Compton W, Gauss 2, and Oppenheimer 3; therefore, the reconstructed surfaces at these sites likely have the largest errors (see section 2.4 for sensitivity analysis of pre-existing surfaces to errors).

Since LPDs are pre-Imbrian (>3.85 Ga) to Imbrian ($\sim$3.85–3.2 Ga) in age (Head, 1974), the effect of regolith development on the albedo and morphology of LPDs must be considered. The model presented by Gault et al. (1974) indicates that a 3.8 Gy aged surface has been turned over at least once to a depth of 1.2 m, 10 times at 70 cm, and 100 times at 10 cm. A 4 Gy surface would have been turned over to a depth of 10 m. Considering the extremely shallow slopes of LPDs, regolith turnover therefore may have dramatically blurred the edges of the deposits, causing the apparent edge of the deposit to become less distinct over time, thereby leading to greater uncertainty as to the true areal extent of the deposit. Without more precise knowledge about regolith development at each site, the importance of its effects on underestimating the volumes and areas measured in this study cannot be quantified.

In short, while estimation of unconstrained error sources is beyond the scope of this study, it is nonetheless important to bear them in mind while reviewing the quantities presented in this study.

2.3. Vent infill

A simple way to estimate the impact of tephra fallback into the vent on our calculations is to model the original vent as a cone and calculate the difference between the idealized cone volume and the measured vent volume. For each vent in our dataset that is symmetric and nearly circular (Compton W, Gauss 1, Lassell H, and all Alphonsus vents except for Alphonsus 1), a cone was constructed with the contour at half-depth of the difference DTM serving as its base. Use of the difference DTM ensures that topographic complexity from pre-existing morphology was excluded. The area

Table 1
Descriptions of exposures of wall rock material within the vents.

Deposit name	Latitude (°N)	Longitude (°E)	Exposure description
Alphonsus 1	−12.51	358.04	Some grain flow patches
Alphonsus 2	−12.54	358.28	Potential outcroppings of discrete surface (Fig. 3a)
Alphonsus 4	−12.86	358.38	Possible surface obscured by creep
Alphonsus 5	−13.09	358.39	No compelling exposures
Alphonsus 6	−13.51	358.55	Fairly consistent max elevation of bright grain flow patches, no structural indication of layer (Fig. 3b)
Alphonsus 7	−14.39	358.09	Some grain flow patches
Alphonsus 8	−13.78	356.62	Possible surface obscured by creep
Alphonsus 9, 10, 11	−13.57	355.92	Discrete surface identified in 11 (Fig. 3b), one surface exposure in 10, grain flow patches in 9
Oppenheimer 1	−33.55	194.52	No compelling exposures
Oppenheimer 2	−37.10	195.42	Bight band of blocky material
Oppenheimer 3	−35.30	196.75	No compelling exposures
Oppenheimer 4	−34.96	196.58	No compelling exposures
Crisium 1	18.55	61.91	No compelling exposures
Crisium 2	19.08	61.20	No compelling exposures
Gauss 1	35.87	76.65	One grain flow feature, no indication of stratigraphical interface
Gauss 2	36.30	81.50	No compelling exposures
Birt E	−20.73	350.36	Possible surface identified
Compton W	54.10	105.39	No compelling exposures
Isis	18.97	27.47	No compelling exposures
Lassell H	−15.00	349.13	No compelling exposures
Osiris	18.64	27.64	No compelling exposures
Schrödinger	−75.40	138.60	Structural indications of interface present on both sides of vent (Fig. 3c)
Tobias Mayer W	19.20	327.50	Possible surface identified

enclosed by the contour at half-depth was segmented radially into 50 slices, whose distances were used to calculate a median distance from the centroid of the contour. The median slope was extracted from along the contour, which was used together with the median distance to model the height of the cone. The volumes of the 50 slices projected to the calculated cone height were calculated and summed. A visual inspection in ArcScene (ESRI, 2011) of the resulting 3D cone along with the original vent in the difference DTM confirmed that the resulting cones are realistic extrapolations of the existing vents.

The disparity in volume between the cone and the difference DTM was then subtracted from V_{vent} and added to $V_{deposit}$ before recalculating % juvenile. For nearly all vents to which this procedure was applied, the decrease in the juvenile estimate was less than 2% total juvenile material. The exception was Alphonsus 8, whose juvenile estimate increased by 5% total juvenile material. This exercise confirms that fallback of tephra into the vent does not lead to significant underestimates in juvenile percent, as long as the slopes at half depth are truly representative of the original post-eruptive vent slopes.

2.4. Outcrops and sensitivity analysis

About half of the vents in this study exhibit linear blocky textures partially down the wall that may be interpreted as exposed outcrops of the sub-deposit bedrock revealing the maximum depth of the overlying pyroclastic deposit (Table 1, Fig. 3). In a few cases, aligned exposures of mass wasting materials sourced from eroding benches indicate a discrete stratigraphic interface interpreted to represent the pre-existing surface. These outcrops present an opportunity to test the aforementioned method of approximating the pre-existing surface.

To investigate the sensitivity of results to estimates of the pre-existing surface, alternative pre-existing surface models were created (referred to as reconstructed surface B) for three deposits containing deliberate topographic modifications representing end-member, but still realistic, cases (Fig. 4). The locations of observed outcrops on the vent walls are then used to show that the surface generated using the methods described in Section 2.1 above (reconstructed surface A) is more likely.

Alphonsus 2

Reconstructed surface A (as shown in Fig. 2) relied heavily on a topographic profile (Fig. 2b) across the deposit and extrapolation from the topography outside of the deposit to a minimum-curvature profile. If this step is removed and it is instead assumed, as an end-member alternative, that the small depression north of the rille sloped up more steeply north of the rille (reconstructed surface B), the difference (thickness) map B is much more irregular than difference map A. Moreover, the locations of blocky outcrops (indicated by black dots) on difference map A are noticeably closer to the plane of 0 thickness (white in the difference/thickness DTM), where the model indicates an interface should be visible. Of the three deposits tested, the difference in the calculated juvenile proportion from reconstructed surface A to reconstructed surface B was the most dramatic for Alphonsus 2, decreasing from 24% to 0%.

Alphonsus 9, 10, 11

For this deposit, there is uncertainty in the shape of the contours on the floor. Reconstructed surface A exhibits contours following the convex shape of the gently sloping larger crater floor toward the east. However, it is also possible that the contours instead more closely follow the shape of the more prominent ridge hugged by the deposit toward the west, in sharp contrast with the larger-scale topography of the crater floor (reconstructed surface B). Reconstructed surface B results in a difference/thickness map that looks rather similar to difference map A, only thicker and more diffusely distributed. The outcrops once again align more favorably with difference map A. Nevertheless, the difference map B yields a juvenile proportion of 78%, versus 57% calculated from difference map A.

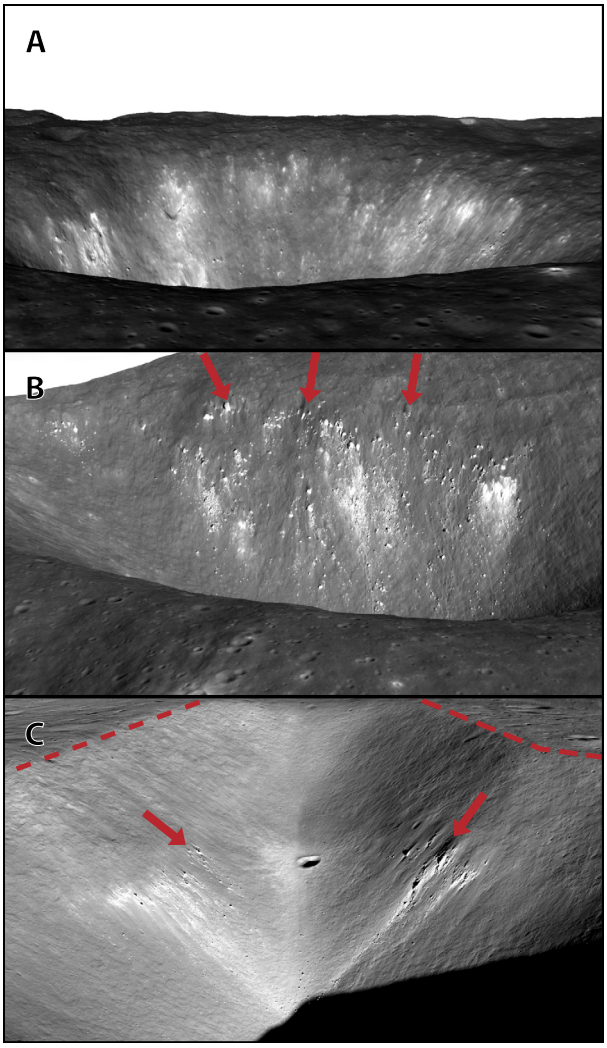

Fig. 3. A) Perspective view of the eastern wall of Alphonsus 6 vent with a series of grain flows of no clear structural origin. The source of erosion in some cases appears to have been overrun by the fine dark deposit material (NAC orthophoto, width of view ~1500 m, vertical exaggeration 2.8x). B) Perspective view of the western wall of Alphonsus 11 vent showing structural benches appearing to source from an interface between the original surface and the deposit (NAC orthophoto, width of view ~1550 m, vertical exaggeration 2.1x). C) Perspective view down the axis of the vent toward the southwest. Red dashes outline the vent rim, which are parallel to linear benches of eroding material on both sides of the vent (indicated by arrows) that likely represent a stratigraphic interface. (NAC image, width of view ~5200 m, vertical exaggeration 1.5x).

Tobias Mayer W

In terms of contextual topography, Tobias Mayer is one of the simplest deposits. Similar to the Alphonsus 9/10/11 deposit, reconstructed surface A has contours following the wide convex downsloping character of the surrounding topography. Therefore, the end-member alternative is an oppositely concave surface (reconstructed surface B). Difference map B once again looks similar to that of difference map A, albeit generally thicker. The exposed outcrops agree with both models roughly equally. This alternative surface example had a smaller impact on the calculated juvenile proportion than was found in the previous two examples, with an increase from A to B of about 14% from 54% to 68%.

These analyses demonstrate the importance of careful consideration of surrounding topography when generating pre-existing surfaces. It shows that in the worst cases, errors in reconstructed surfaces may be as high as ±25%.

3. Results

Fig. 5 is a graphic table of reconstructed pre-existing surfaces (equivalent to surface A in Fig. 4) for each LPD and their resulting difference maps. Volume measurements, calculated juvenile volumes and percentages, and other morphometric measurements and calculations can be found in Table 2. The average deposit thicknesses at the vent were calculated by averaging the thickness values along the apex of the vent rim. The overall average deposit thickness is the volume of the deposit divided by the area of the deposit (vent area subtracted). Deposits containing multiple vents were treated as a single deposit when calculating the juvenile content, with V_{vent} being the sum of the individual vent volumes. Although the deposit volumes for all other multi-vent deposits were combined, vent depths and deposit thicknesses immediately surrounding the vents were still performed on an individual basis and are presented as multiple values for their respective deposits.

Results show a wide variety of morphometric characteristics among deposits, with juvenile proportions spanning the entire range of 0–100%. There were four deposits that returned negative percent juvenile values for some or all bedrock densities considered. Oppenheimer 4 and Alphonsus 2, 4, 5, and 8 exhibit error bars extending below 0 for the higher density ranges. Alphonsus 6, however, returned negative values for all densities considered. This is not fully explained by the exclusion of the large cavity in the northern portion of the current surface from its pre-existing surface model, since the percent juvenile estimate is still negative when the southern half of the deposit and vent are measured. Therefore, the volume of Alphonsus 6 is an underestimate. The return of negative juvenile percent values for greater bedrock densities for these five deposits, which are the smallest deposits by nearly every measure, may indicate that deposit volumes are being systematically underestimated or that sensitivity to error is inversely proportional to deposit size. This may be partially explained by the fact that NAC DTM vertical uncertainties are agnostic to deposit size and thus have a disproportionately large impact on the size of errorbars for small deposits. Systematic underestimates may be due to muting of the landscape during regolith development (including fallback of material into the vent), or they may indicate that the density contrast between the country rock and deposit is better represented by the smaller of the range of values, or both.

4. Discussion

4.1. Morphometric relationships

Fig. 6 shows the relationships between the calculated volume/proportion of juvenile material and the morphometric properties for each deposit presented in Table 2. There is a weak positive logarithmic relationship between the proportion of juvenile material and both total deposit volume (Fig. 6b, unweighted $R^2 = 0.72$) and area (Fig. 6d, unweighted $R^2 = 0.56$) for deposits containing less than ~80% juvenile material. Interestingly, deposits situated in inter-crater settings span the entire range of juvenile proportions from 0 to 100%, whereas deposits on the mare tend to contain over 90% juvenile material (the only exception being Tobias Mayer W). These relationships are much tighter and more consistent for absolute juvenile volume (Fig. 6a, unweighted $R^2 = 0.96$ and Fig. 6c, unweighted $R^2 = 0.78$, respectively). The relationship between vent depth and percent juvenile material (Fig. 6f), on the other hand, appears to be positive for deposits composed of less than 50% juvenile material and negative for deposits composed of greater than 50% juvenile material.

The maximum vent depth and the absolute juvenile volume of Alphonsus deposits appear to be tightly positively correlated

Table 2
Volume measurement results and calculations. Cells with multiple values are reporting the values for each vent within a multi-vent deposit. The ranges presented for % juvenile account for variations in bedrock density and LOLA uncertainties alone, and do not represent statistical uncertainties.

Deposit name	Area (km^2)	Deposit volume (km^3)	Vent volume (km^3)	Juvenile volume (BRE) (km^3)	% Juvenile	Maximum deposit thickness (m)	Average deposit thickness at vent (m)	Maximum vent depth (m)	Average deposit thickness (m)	Notes
Alphonsus 1	35	0.416 ± 0.088	0.146 ± 0.005	0.094 ± 0.087	30.4 ± 25.9	74 ± 3	31 ± 3	187 ± 3	12 ± 3	MD Ravi (Head and Wilson, 1979)
Alphonsus 2*	20	0.212 ± 0.049	0.083 ± 0.003	0.043 ± 0.043	25.9 ± 25.9	49 ± 3	36 ± 3	193 ± 3	11 ± 3	Monira (Head and Wilson, 1979)
Alphonsus 4*	46	0.723 ± 0.117	0.286 ± 0.007	0.128 ± 0.128	23.9 ± 23.9	85 ± 3	42 ± 3	311 ± 3	17 ± 3	KC Soraya (Head and Wilson, 1979)
Alphonsus 5*	6	0.030 ± 0.014	0.024 ± 0.002	0.003 ± 0.003	10.7 ± 10.7	23 ± 3	13 ± 3	93 ± 3	6 ± 3	
Alphonsus 6*	11	0.090 ± 0.030	0.092 ± 0.004	0	0	29 ± 3	20 ± 3	185 ± 3	9 ± 3	
Alphonsus 7	71	1.022 ± 0.106	0.343 ± 0.005	0.238 ± 0.144	37.1 ± 15.9	72 ± 2	50 ± 2	272 ± 2	15 ± 2	R (Head and Wilson, 1979)
Alphonsus 8*	18	0.117 ± 0.033	0.069 ± 0.003	0.015 ± 0.015	15.3 ± 15.3	36 ± 2	18 ± 2	139 ± 2	7 ± 2	
Alphonsus 9, 10, 11	92	2.134 ± 0.177	0.264 ± 0.005, 0.065 ± 0.002, 0.170 ± 0.003	0.710 ± 0.277	56.4 ± 10.5	107 ± 2	55 ± 2, 54 ± 2, 83 ± 2	290 ± 2, 145 ± 2, 246 ± 2	25 ± 4	CA (Head and Wilson, 1979)
Oppenheimer 1	70	2.134 ± 0.227	0.157 ± 0.010	1.055 ± 0.304	86.0 ± 4.2	163 ± 3	80 ± 3	116 ± 3	32 ± 3	Oppenheimer N (Bennett et al., 2016)
Oppenheimer 2	35	0.588 ± 0.058	0.109 ± 0.007, 0.076 ± 0.004	0.148 ± 0.090	40.3 ± 17.4	107 ± 2	75 ± 2, 27 ± 2	110 ± 2, 86 ± 2	20 ± 2	Oppenheimer SSE (Bennett et al., 2016)
Oppenheimer 3	40	1.522 ± 0.073	0.028 ± 0.002	0.830 ± 0.162	96.6 ± 0.9	147 ± 2	91 ± 2	58 ± 2	39 ± 2	Oppenheimer E (not to be confused with Opp. E Crater) (Bennett et al., 2016)
Oppenheimer 4*	5	0.035 ± 0.008	0.020 ± 0.002	0.005 ± 0.005	16.3 ± 16.3	31 ± 2	15 ± 2	70 ± 2	9 ± 2	
Crisium 1	33	1.242 ± 0.044	0.004 ± 0.001	0.553 ± 0.080	99.2 ± 0.3	185 ± 1	92 ± 1	20 ± 1	39 ± 1	
Crisium 2	12	0.219 ± 0.012	0.006 ± 0.001	0.093 ± 0.018	93.6 ± 1.8	85 ± 1	46 ± 1	37 ± 1	19 ± 1	
Gauss 1	87	2.982 ± 0.330	0.042 ± 0.006	1.653 ± 0.424	97.3 ± 1.0	136 ± 4	97 ± 4	100 ± 4	35 ± 4	Gauss W (not to be confused with Gauss W Crater) (Gaddis et al., 2003)
Gauss 2	108	5.165 ± 0.240	0.712 ± 0.017, 0.076 ± 0.004	2.122 ± 0.560	71.8 ± 5.8	195 ± 2	137 ± 2, 48 ± 2	296 ± 2, 127 ± 2	51 ± 2	Gauss E (not to be confused with Gauss E Crater) (Gaddis et al., 2003)
Birt E†	356	14.856 ± 1.176	0.554 ± 0.016	6.148 ± 1.330	91.3 ± 1.9	214 ± 2	160 ± 2	173 ± 2	43 ± 3	Large deposit only (small northeastern deposit excluded from calculations)
Compton W	15	0.420 ± 0.040	0.080 ± 0.004	0.158 ± 0.059	64.0 ± 10.0	104 ± 3	75 ± 3	155 ± 3	31 ± 3	
Isis	6	0.098 ± 0.030	0	0.045 ± 0.019	100	77 ± 5	56 ± 5	0	16 ± 5	
Lassell H	7	0.333 ± 0.019	0.001 ± 0.0003	0.149 ± 0.026	99.3 ± 0.3	158 ± 3	118 ± 3	19 ± 3	46 ± 3	
Osiris	5	0.151 ± 0.027	0	0.069 ± 0.020	100	102 ± 5	78 ± 5	0	28 ± 5	
Schrodinger	877	103.320 ± 1.516	3.326 ± 0.019	54.760 ± 9.844	94.1 ± 1.1	496 ± 3	436 ± 3	591 ± 3	120 ± 2	
Tobias Mayer W	232	4.985 ± 0.613	0.992 ± 0.012	1.269 ± 0.550	53.4 ± 11.6	110 ± 2	78 ± 2	360 ± 2	22 ± 3	

† Note that while Birt E is a multi-vent deposit, NAC DTM coverage does not include the smaller northwestern vent, thus its volume has been excluded from the numbers for Birt E.
* Negative values in juvenile range are reported as 0. Actual calculated juvenile percent and juvenile volume values are, respectively: 21.0 ± 30.8, 0.039 ± 0.047; 23.7 ± 24.1, 0.127 ± 0.128; −113.5 ± 134.8, −0.006 ± 0.012; −123.4 ± 107.8, −0.040 ± 0.028; −23.7 ± 54.4, −0.001 ± 0.030; −19.1 ± 51.6, 0 ± 0.009.

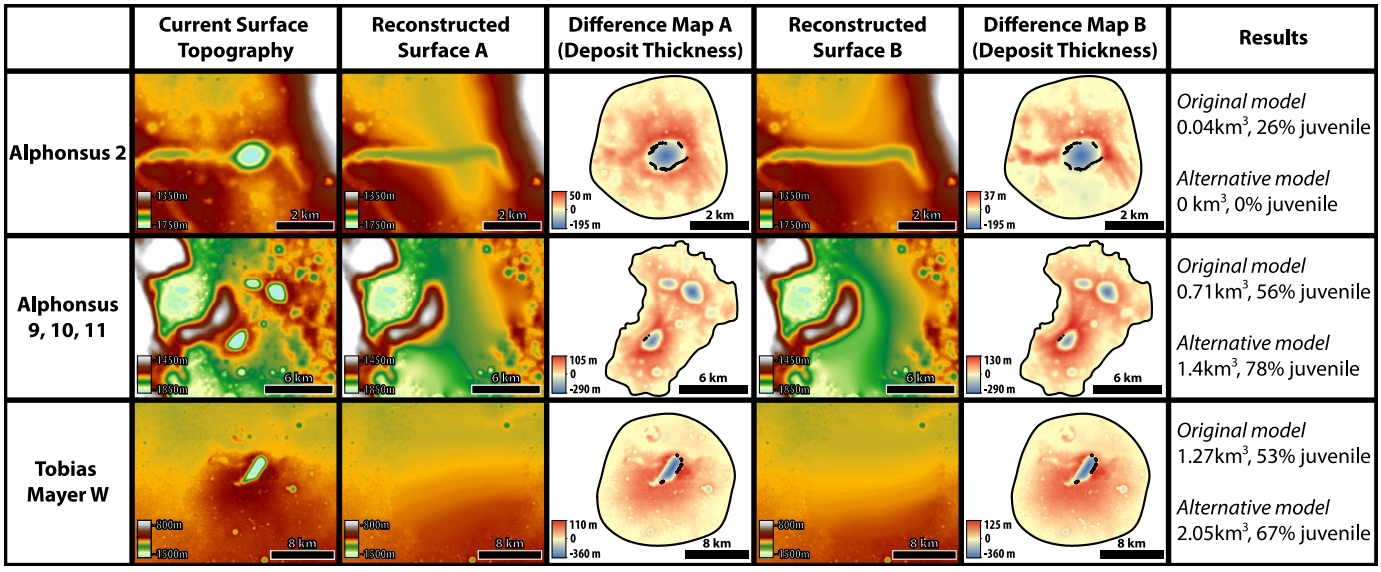

Fig. 4. Summary table of the results of the sensitivity of the calculations in this study to changes in the shape of pre-existing surface models. Alternative surfaces are designed to represent extreme, yet realistic, cases (reconstructed surface B). Black dots denote locations of identified outcrops interpreted as marking the interface between the deposit and the underlying country rock; they broadly agree more with the original model surfaces (reconstructed surface A) produced following the methods employed in this study.

(Fig. 6e). The remaining vent depths also show a positive correlation with absolute juvenile volume, but they do not fall on the same trend and are generally more scattered. Maximum deposit thickness (Fig. 6g, h), average deposit thickness near the vent (Fig. 6i,j), and average overall thickness (Fig. 6k,l) are all positively correlated with total juvenile volume and juvenile percentage. Although there is some clustering of deposits from the same locations on these charts, particularly the Alphonsus deposits, geomorphic characteristics do not appear to be strongly dictated by location. Instead, the relationships suggest that LPD deposit size is controlled by the absolute volume and proportion of juvenile magma that participated in the eruption. While the observation by Head and Wilson (1979) that the deposits at Alphonsus Crater are low in juvenile content is generally consistent with the measurements reported here, it appears that those deposits represent only part of a larger morphometric trend for localized pyroclastic deposits.

4.2. Comparison with remote sensing studies

Spectral observations from the Moon Mineralogy Mapper (M^3) aboard Chandrayaan-1 (Pieters et al., 2009) and the Diviner Lunar Radiometer Experiment aboard the Lunar Reconnaissance Orbiter (Paige et al., 2010) together allow for much more precise measurement of iron-bearing minerals and glasses compared to Clementine-based results. Using these datasets, Bennett et al. (2016) found that the Oppenheimer 1 and 3 deposits bear strong glass signatures with traces of clinopyroxene (interpreted as juvenile material), with Oppenheimer 3 in particular exhibiting spectral characteristics suggesting that it is nearly entirely composed of glass, consistent with the morphometric-based estimates presented here that indicate the deposits are almost entirely juvenile. On the other hand, Oppenheimer 2 was found by Bennett et al. (2016) to be a mixture of glass and clinopyroxene, which conflicts with our results indicating that Oppenheimer 2 is composed of a roughly equal mixture of juvenile material (glass and clinopyroxene) and crater floor material (orthopyroxene). However, failure to detect orthopyroxene by spectral methods does not necessarily indicate its absence in the deposit, only that it is probably not present in detectable quantities on the surface of the deposit (i.e., late stage erupted products might be entirely juvenile). Finally, Oppenheimer 4 was only faintly detectable in glass band depth parameters (Bennett et al., 2016), suggesting that it contains very little glass, though with a surface area of only 5 km^2, it may simply be too small for a signature to be visible through the noise in their M^3 glass band depth map.

Gaddis et al. (2016) also used M^3 data to analyze the deposits in Alphonsus crater. Their findings indicate that all of the deposits in the crater are orthopyroxene-rich, but the largest deposits (Alphonsus 1, 4, 7, 9, 10, and 11) also contain mixtures of clinopyroxene and glass. In particular, the western cluster of vents (9–11) contain a significant glass+orthopyroxene component, particularly near the southern deposit (11). Another recent study (Allen et al., 2013) applying M^3 and Diviner data to LPDs in Alphonsus Crater found elevated abundances of FeO in the deposits (13.8 $\pm$ 3.3 wt.%) compared to that of the crater floor material (7.5 $\pm$ 1.4 wt.%) yet within the range of iron oxide abundances measured in pyroclastic glasses (Papike, 1998). The results of these studies are consistent with the results of this study, which show very little to no juvenile material for the smallest deposits (by area) and moderate to significant juvenile component (~20–60%) for the larger deposits in Alphonsus crater.

Finally, Besse et al. (2014) found using M^3 data that the deposit at Birt E has a signature indicating a mixture of glass with a basaltic component. Since the deposit is located within a mare basalt unit, the source of its basaltic component may be the country rock or crystalline juvenile material from the same eruption(s) that produced the glassy material. This study's estimate of ~89–93% juvenile material suggests the latter as the primary source of the signature.

4.3. Eruption dynamics

The observation that mare LPDs tend to be juvenile-rich while floor-fractured crater LPDs vary widely hints at a commonality in mare settings that is not necessarily shared by all floor-fractured crater settings. Crustal thickness values at each deposit location (Supplemental Table 1) retrieved from a lunar crustal thickness map presented by Wieczorek et al. (2013) do not directly correlate to results for juvenile percent, juvenile volume, nor any other morphometric parameter presented in Table 2. Juvenile rich deposits in mare settings may instead be a result of factors more

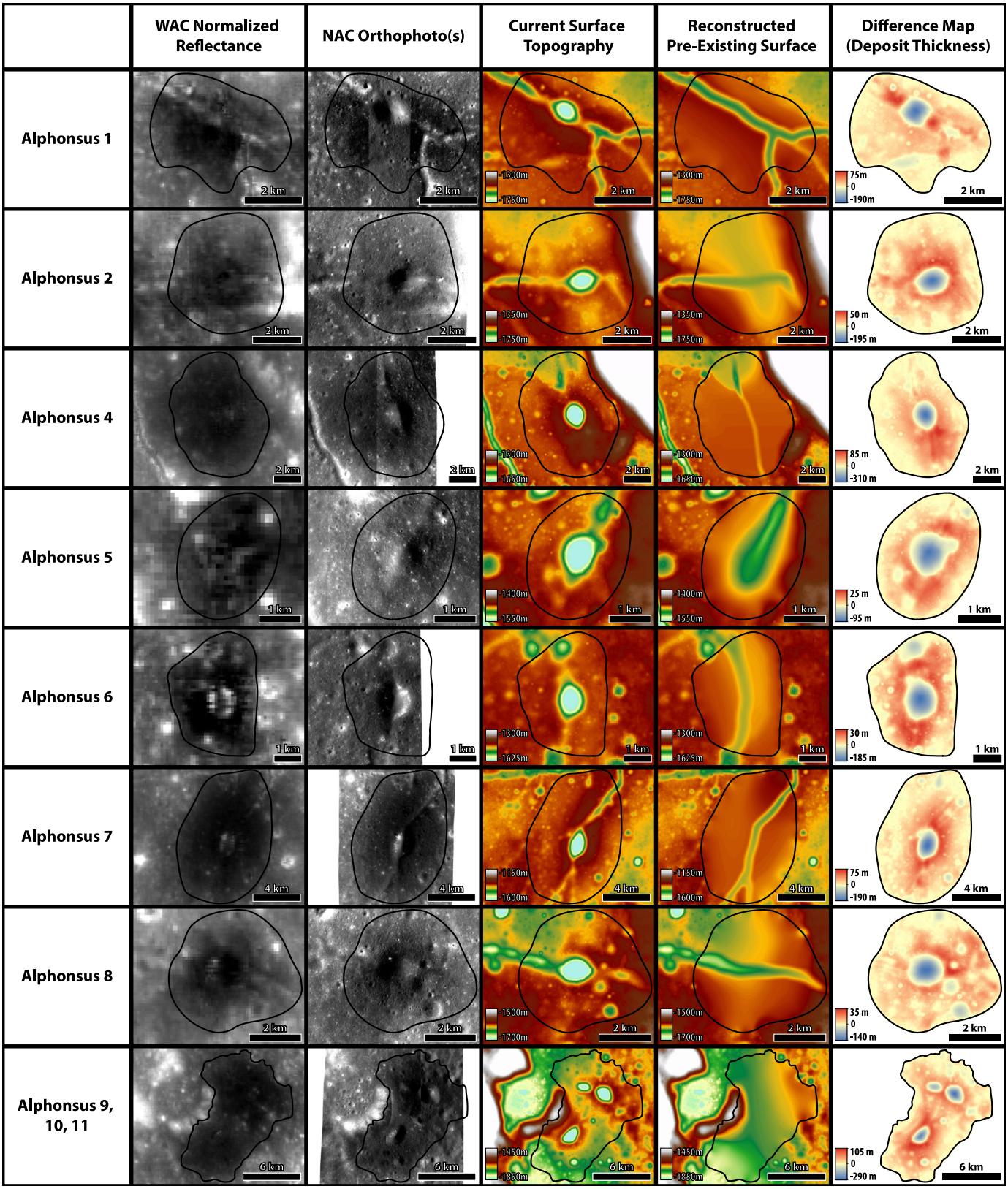

Fig. 5. Graphic tables presenting the current surface appearance and topography of the LPDs in this study alongside the pre-existing surface model and the difference/deposit thickness DTM corresponding to each deposit. Areas not covered by NAC DTMs are filled in with the WAC-Kaguya global DTM. NAC DTM coverage is equal to the orthophoto coverage shown in the second column.

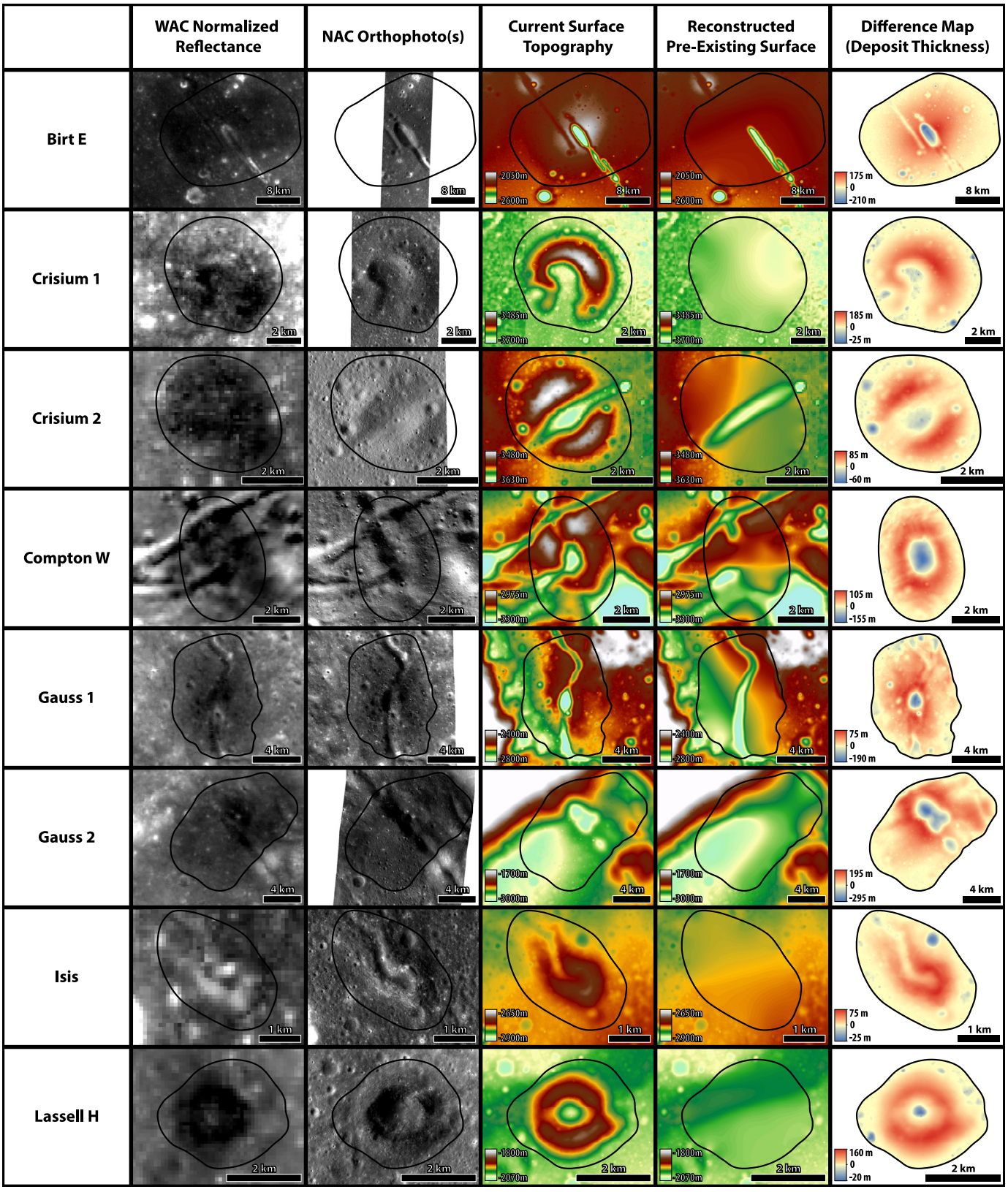

Fig. 5. (*continued*)

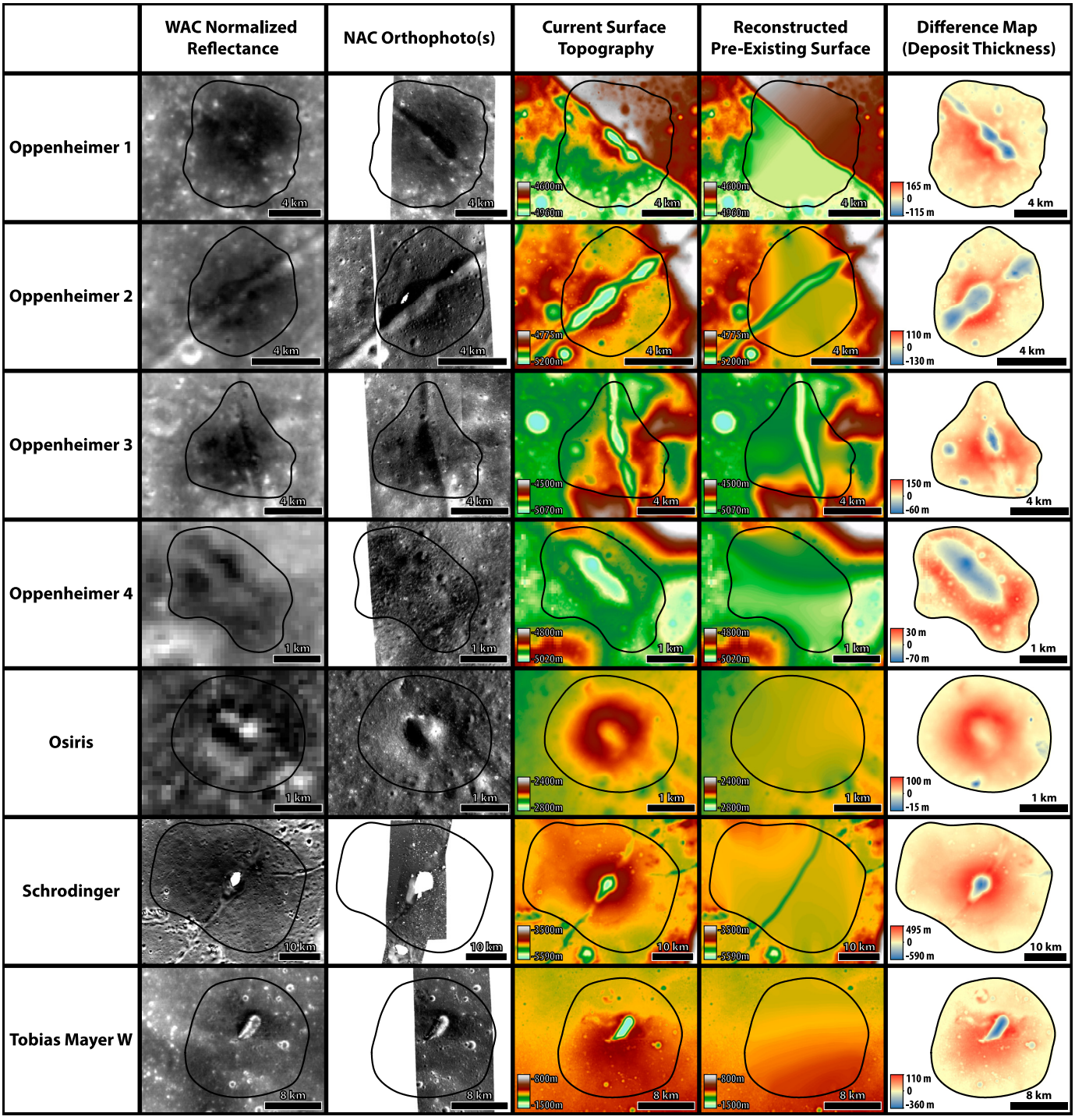

Fig. 5. (*continued*)

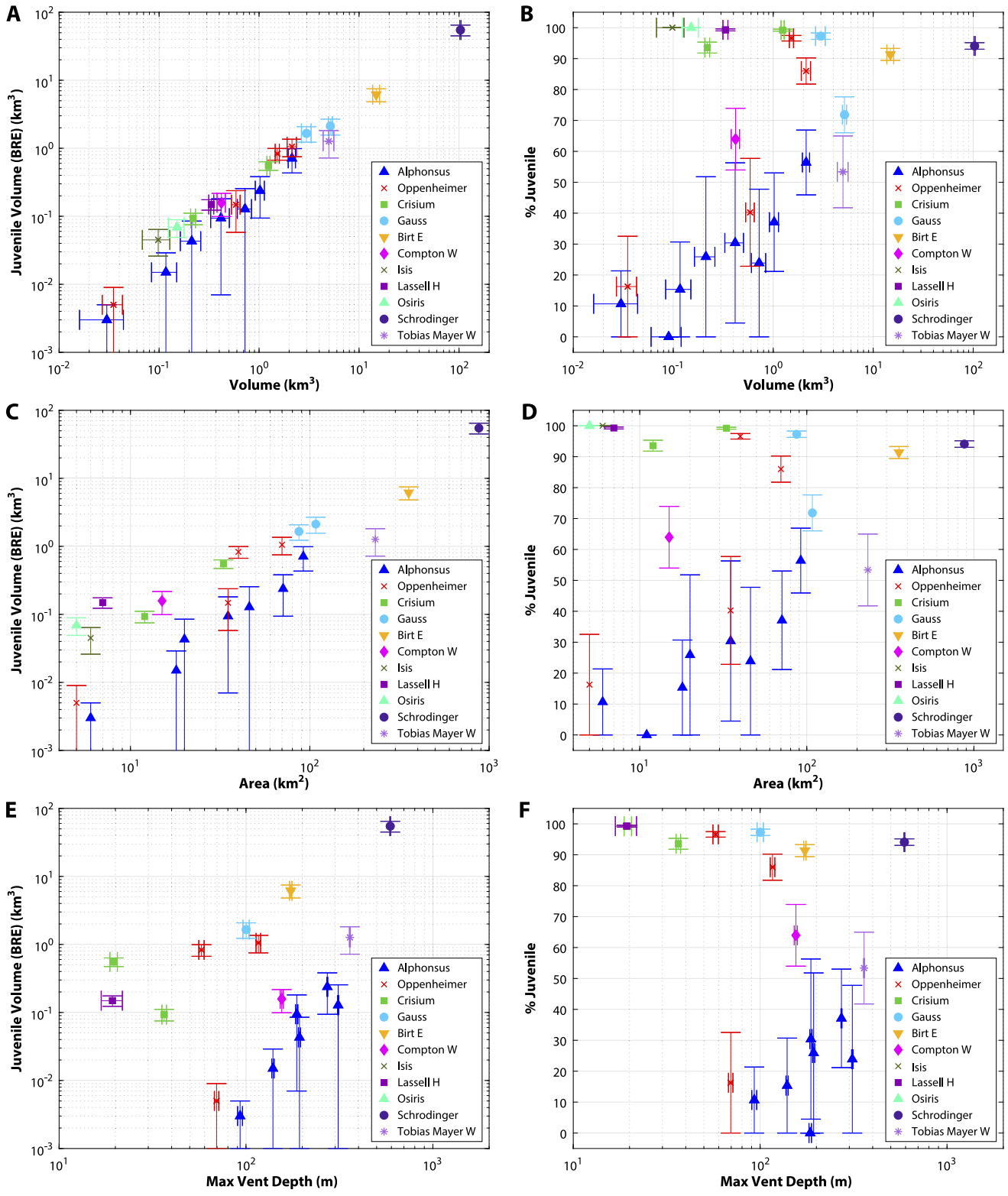

Fig. 6. Plots depicting relationships between juvenile volume/proportion and various morphometrics. Vertical errors are derived from the range of expected bedrock and deposit densities and the volume errors calculated using the vertical precision of the DTMs. Horizontal uncertainties are derived from the latter alone. Multi-vent deposits are not plotted in max vent depth nor average thickness near vent since each deposit contains multiple values for those metrics. Note that the negative portions of the % juvenile ranges for Oppenheimer 4 and Alphonsus 2, 4, 5, 6, and 8 are interpreted as 0 and therefore are not shown. See Table 2 footnote for actual calculated values.

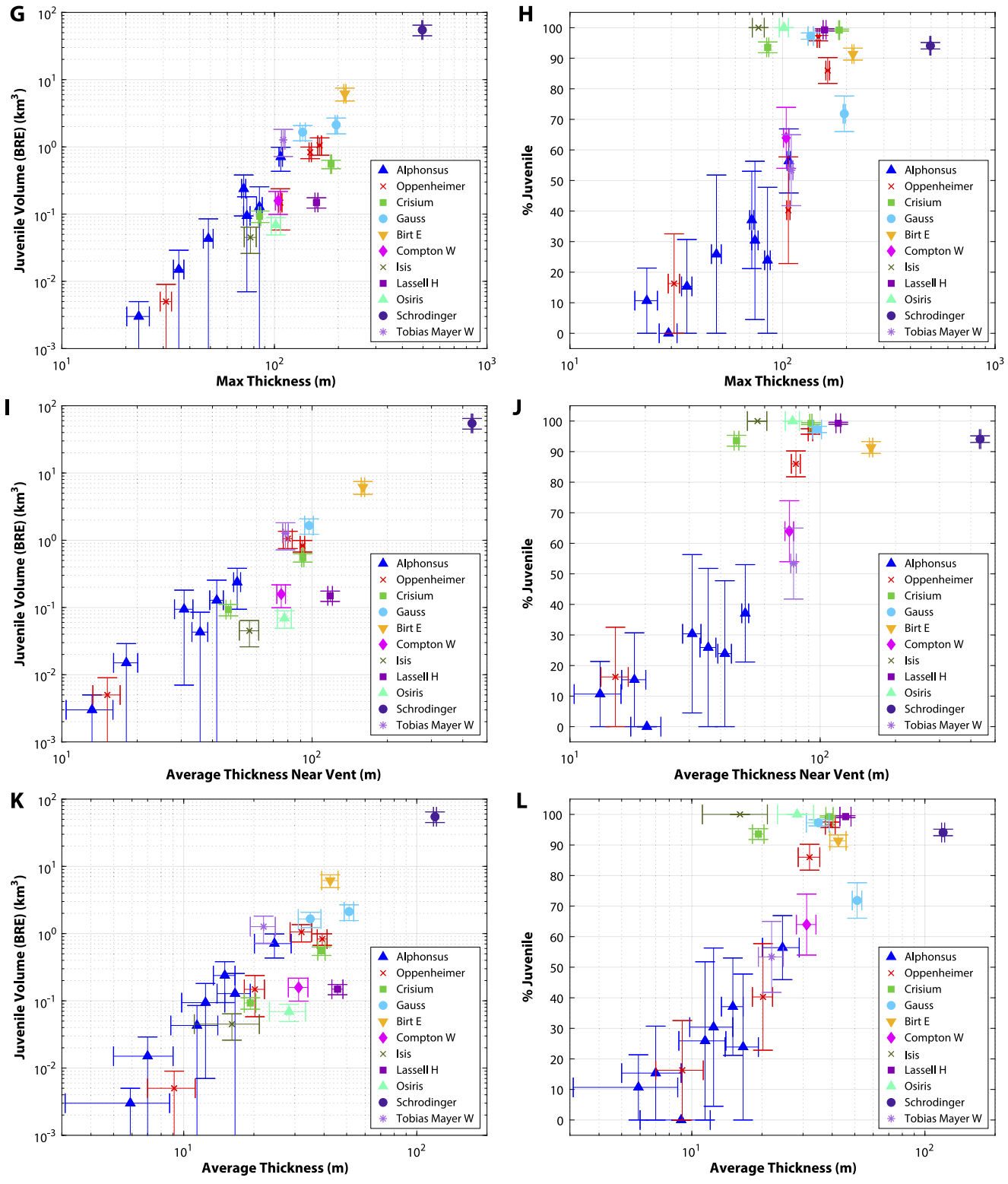

Fig. 6. (*continued*)

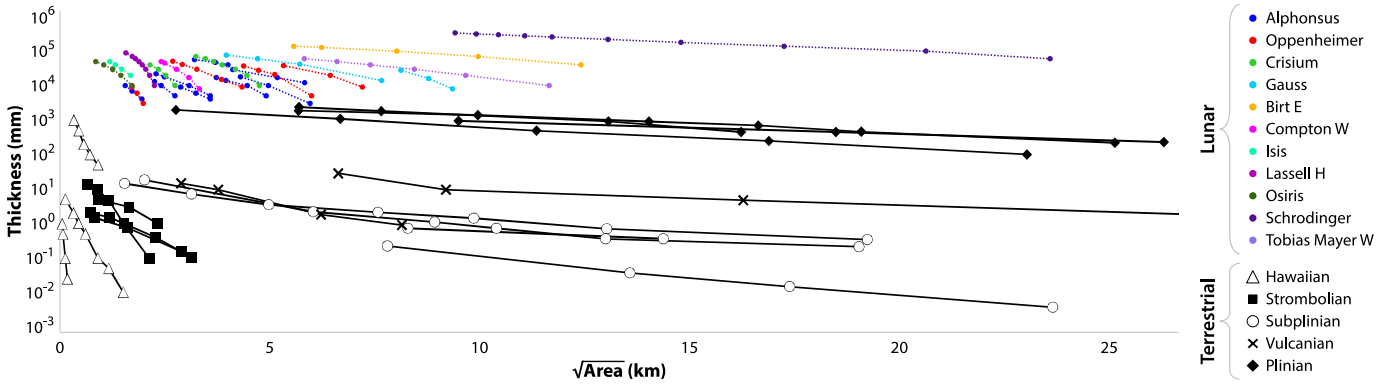

Fig. 7. Thinning trends for deposits in this study alongside thinning profiles from terrestrial deposits of known eruption type (Bonadonna et al., 2002; Houghton and Gonnermann, 2008; Houghton and Carey, 2015; Taddeucci et al., 2015; Romero et al., 2017).

difficult to measure directly, such as characteristics of the magma and magma plumbing systems feeding the eruptions, or age differences between deposits.

It has long been thought that cones, localized dark mantle deposits, and regional dark mantle deposits represent separate eruption mechanisms and have thus been treated as separate classes of pyroclastic deposits with distinct eruption models (e.g., Head and Wilson, 1979, 2017). However, recent spectral studies of LPDs have uncovered wider compositional diversity among deposits than previously postulated (e.g., Gaddis et al., 2000, 2003; Besse et al., 2014; Jawin et al., 2015; Bennett et al., 2016). The slow ascent rates associated with the simple lunar Vulcanian model would hinder the eruption of large quantities of juvenile material, yet glass and clinopyroxene have been identified in small to moderate amounts at Alphonsus Crater (Jawin et al., 2015; Gaddis et al., 2016) and in moderate to large amounts at Oppenheimer Crater (Bennett et al., 2016). Fig. 7 shows the thinning trends of the deposits in this study, where each point represents the square root of the area enclosed by the corresponding isopach (i.e., thickness contour), alongside terrestrial deposits produced by various eruptive mechanisms. This method of plotting profiles of pyroclastic deposits was first implemented by Walker (1973) and is most often used by terrestrial volcanologists to calculate deposit volumes using, for example, methods described by Pyle (1989). However, the slope of the thinning profile has also been correlated with eruption type (e.g., Houghton et al., 2000; Houghton and Gonnermann, 2008; Bonadonna and Costa, 2009; Houghton and Carey, 2015). The lunar data in Fig. 7 was generated by plotting isopachs using the difference DTM for each deposit and calculating the enclosed area for several thicknesses at different distances from the vent. The lunar profiles are consistently thicker than their terrestrial counterparts, suggesting that they may be polygenetic or that they underwent longer eruption durations than is typical for analogous eruption types on Earth. The slopes vary from steep (similar to Strombolian-type on Earth) to very shallow (matching Plinian-type on Earth). Interestingly, deposits from the same sites appear to exhibit similar slopes to one another despite having different juvenile proportions, perhaps implying that eruptions occurring near one another share eruption rates and style, but not necessarily eruption durations and volumes.

Fundamental differences between eruptive environments of the Earth and the Moon, most importantly the presence of an atmosphere on Earth that allows for the formation of tall convective columns, make direct correlations of eruption styles between the two bodies problematic. However, the broad range of profile slopes, along with the diversity of morphometric relationships shown in Fig. 6 and observations of compositional diversity among LPDs in previous studies, suggest that no single eruptive mechanism or single eruption scale could have created all of the deposits. Furthermore, the results show that deposits termed cones in the literature (Crisium 1 and 2, Isis, Osiris, and Lassell H) and deposits termed localized dark mantle deposits (all others) fall along a common morphological continuum, with no clear separation between the two groups. Therefore, we here propose that the current models for LDMDs and cones be treated as end-member scenarios, with the Alphonsus deposits representing lunar Vulcanian deposits, cones representing Hawaiian or Strombolian deposits, and most others forming a transitional regime, with Vulcanian-type depressurization followed by Hawaiian or pure-jet subplinian-scale eruptions of varying energies (as suggested by Bennett et al., 2016). Variations in size and juvenile content among LPDs may be due to differences in eruption durations and local variations in ascent rate due to differences in subsurface fracture widths, subsurface storage depths and pressures, and magma volatile contents.

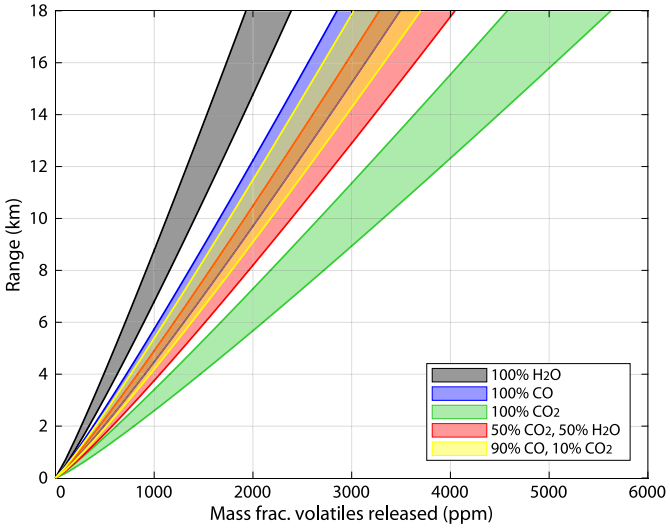

Fig. 8. Ranges of ejected 0.03–0.3 mm pyroclasts for a 1500 K magma and multiple gas compositions calculated using equations from Wilson and Head (2017). See Section 4.3: Eruption dynamics for complete list of input parameters.

A model developed by Wilson and Head (2017) for lunar eruptions considers magma ascent, vesiculation, fragmentation, and ballistic emplacement of tephra in a vacuum. Fig. 8 plots results of that model for a range of possible volatile contents responsible for producing the footprints of the deposits in this study, which have a maximum range of about 17 km. In these runs, a magma density of 2900 kg/m^3, a crustal density of 2550 kg/m^3, a magma temperature of 1500 K, a range of particle diameters of 0.3–3 mm, and a range of dissolved magmatic volatile contents and compositions as illustrated in Fig. 8 were used. Results suggest that the volatile contents may have been very high for the widest deposits,

between ~2000 ppm and ~5000 ppm, depending on gas composition. These values roughly agree with findings from Hauri et al. (2011), who measured up to 1410 ppm of water in olivine-hosted melt inclusions in Apollo 17 glass beads. Given the lower solubility of CO_2 and CO in basalt compared to water, it is likely that those species had been exsolved prior to formation of the melt inclusions in the Hauri et al. (2011) study. It is therefore reasonable to surmise that the total fraction of volatiles dissolved in the magma at depth was greater by a nontrivial amount. Fig. 8 also highlights the significance of gas composition in determining eruption explosivity. To what extent gas composition varied in lunar magmas, and what role any diversity in gas compositions may have had in producing the variety of volcanic landforms observed today is a subject worthy of future investigation.

As a final note, the lunar community is urged to develop new terms for lunar eruption types that are independent of terrestrial eruption types, as the application of terrestrial terms to lunar eruptions is often misleading, particularly for terrestrial workers accustomed to strict definitions for eruption types on Earth.

5. Summary and conclusions

The results of analysis of 23 localized pyroclastic deposits (LPDs) can be summarized by the following:

1. LPDs have a much wider range of juvenile fractions than previously recognized. There is a broadly positive relationship between various morphometrics (most notably deposit thickness and deposit area) and juvenile content of LPDs, both in terms of juvenile proportion and total juvenile volume.
2. The range of estimates for Alphonsus generally agree with those from Head and Wilson (1979), with juvenile contents ranging from 0 to 60%. However, other deposits previously hypothesized to contain similarly low juvenile proportions to the Alphonsus deposits are estimated to contain as much as 97% juvenile material. Aside from Tobias Mayer W and two Oppenheimer deposits, all other deposits analyzed in this study contain more than 60% juvenile material. The juvenile volume of many of these deposits is also estimated to be quite high. Most fall in the range of 0.05–1 km^3 bedrock-equivalent volume, but the largest, Schrödinger, contains over 50 km^3, which is of particular interest for future in-situ resource extraction applications (e.g., Hawke et al., 1990).
3. Observations combined with dynamic modeling suggest that the juvenile magma involved in many of these eruptions had significant dissolved volatile fractions. This finding, along with the large volumes of juvenile material also documented here, suggests that the total quantity of volatiles released from these eruptions is larger than previously thought, generally ranging 10^7–10^{10} (but as high as 10^{11}) kg per deposit, based on total juvenile magma volumes (BRE) and the median of volatile contents required to explain pyroclast ranges (Fig. 8).
4. LPDs bear a wide range of thinning relationships that would span multiple eruption styles on Earth. These data suggest that a single formative mechanism hypothesis is not sufficient to explain the morphometry of all LPDs. Additionally, a range of slopes are represented, spanning the relatively flat Alphonsus deposits to the steeper cones such as Lassell H, instead of clustering into two distinct groups. The existence of a continuum between localized dark mantle deposits and cones in terms of morphometrics and juvenile proportion suggests that they represent a range of related eruptive behaviors between two end-members.
5. Comparison of lunar thinning profiles with terrestrial profiles reveals that the lunar deposits in this study are thicker than terrestrial deposits. This comparison may suggest that some lunar eruptions were polygenetic or that they formed by longer eruptions, and possibly reflect differences in eruption dynamics between bodies with and without an atmosphere.
6. Previous studies of the glass and mineralogic estimates of LPDs have found greater quantities of juvenile material and overall compositional diversity among deposits than expected. These observations combined with the results of this study show that LPDs represent a range of eruptive behaviors and thus call for more complex modeling of eruption mechanisms including style transitions, for example. Finally, the consistency of our results with remote sensing studies validate the use of morphometry to estimate the juvenile composition of LPDs.

Declaration of competing interest

The authors declare that they have no known competing financial interests or personal relationships that could have appeared to influence the work reported in this paper.

Acknowledgements

This work was supported by the NASA LRO project (grant number NNG07EK00C) and the NSF GRFP (grant number DGE-1311230). We extend our deepest thanks to Megan Henriksen, Madeleine Manheim, and the rest of the LROC SOCETSET team for making it possible to produce the high-quality DTMs used in this work. We would also like to thank the LROC team as a whole for efforts toward providing the data products used in this work and for scientific feedback during its progress. Finally, we thank the anonymous reviewers and editor whose comments have strengthened this manuscript.

Appendix A. Supplementary material

Supplementary material related to this article can be found online at https://doi.org/10.1016/j.epsl.2020.116426.

References

Alfano, F., Ort, M.H., Pioli, L., Self, S., Hanson, S.L., Roggensack, K., Allison, C.M., Amos, R., Clarke, A.B., 2019. Subplinian monogenetic basaltic eruption of Sunset Crater, Arizona, USA. Geol. Soc. Am. Bull. 131 (3–4), 661–674. https://doi.org/10.1130/B31905.1.

Allen, C.C., 2015. Taurus Littrow pyroclastic deposit: high-yield feedstock for lunar oxygen. In: Proceedings of the 46th Lunar and Planetary Science Conference, p. 1140.

Allen, C.C., Donaldson-Hanna, K.L., Pieters, C.M., Moriarty, D.P., Greenhagen, B.T., Bennett, K.A., Kramer, G.Y., Paige, D.A., 2013. Pyroclastic deposits in floor-fractured craters – a unique style of lunar basaltic volcanism? In: Proceedings of the 44th Lunar and Planetary Science Conference, p. 1220.

Barker, M.K., Mazarico, E.M., Neumann, G.A., Zuber, M.T., Haruyama, J., Smith, D.E., 2016. A new lunar digital elevation model from the lunar orbiter laser altimeter and SELENE terrain camera. Icarus 273, 346–355. https://doi.org/10.1016/j.icarus.2015.07.039.

Bennett, K.A., Horgan, B.H.N., Gaddis, L.R., Greenhagen, B.T., Allen, C.C., Hayne, P.O., Bell, J.F., Paige, D.A., 2016. Complex explosive volcanic activity on the Moon within Oppenheimer crater. Icarus 273, 296–314. https://doi.org/10.1016/j.icarus.2016.02.007.

Besse, S., Sunshine, J.M., Gaddis, L.R., 2014. Volcanic glass signatures in spectroscopic survey of newly proposed lunar pyroclastic deposits. J. Geophys. Res., Planets 119 (2), 355–372. https://doi.org/10.1002/2013JE004537.

Bonadonna, C., Costa, A., 2009. Modeling tephra sedimentation from volcanic plumes. In: Lopes, R. (Ed.), Modeling Volcanic Processes: the Physics and Mathematics of Volcanism. Cambridge University Press, Cambridge, pp. 173–202.

Bonadonna, C., Mayberry, G.C., Calder, E.S., Sparks, R.S.J., Choux, C., Jackson, P., Lejeune, A.M., Loughlin, S.C., Norton, G.E., Rose, W.I., Ryan, G., Young, S.R., 2002. Tephra fallout in the eruption of Soufriere Hills volcano, Montserrat. In: Druitt, T.H., Kokelaar, B.P. (Eds.), The Eruption of Soufriere Hills Volcano, Montserrat, from 1995 to 1999. Mem. Geol. Soc. Lond. 21, 483–516.

Boyd, A.K., Nuno, R.G., Robinson, M.S., Denevi, B.W., Hapke, B.W., 2013. LROC WAC 100 meter scale photometrically normalized map of the Moon. In: American Geophysical Union Fall Meeting Abstracts.

Carr, M.H., 1996. Geologic Map of the Mare Serenitatis Region of the Moon. USGS Misc. Invest. Map i-489, U.S. Geological Survey, Reston, Va.

Costantini, L., Bonadonna, C., Houghton, B.F., 2009. New physical characterization of the Fontana Lapilli basaltic Plinian eruption, Nicaragua. Bull. Volcanol. 71, 337–355. https://doi.org/10.1007/s00445-008-0227-9.

El-Baz, F., 1972. The cinder field of the Taurus Mountains, part I. Apollo 15 Preliminary Science Report, NASA SP-289.

ESRI, 2011. ArcGIS Desktop: Release 10. Environmental Systems Research Institute, Redlands, CA.

Gaddis, L.R., Hawke, B.R., Robinson, M.S., Coombs, C.R., 2000. Compositional analyses of small lunar pyroclastic deposits using Clementine multispectral data. J. Geophys. Res., Planets 105 (E2), 4245–4262. https://doi.org/10.1029/1999JE001070.

Gaddis, L.R., Horgan, B.H.N., McBride, M., Bennett, K.A., Stopar, J.D., Gustafson, J.O., 2016. Alphonsus crater: compositional clues to eruption styles of lunar small volcanoes. In: Proceedings of the 47th Lunar and Planetary Science Conference, 2065.

Gaddis, L.R., Pieters, C.M., Hawke, B.R., 1985. Remote sensing of lunar pyroclastic mantling deposits. Icarus 61 (3), 461–489. https://doi.org/10.1016/0019-1035(85)90136-8.

Gaddis, L.R., Staid, M.I., Tyburczy, J.A., Hawke, B.R., Petro, N.E., 2003. Compositional analyses of lunar pyroclastic deposits. Icarus 161 (2), 262–280. https://doi.org/10.1016/S0019-1035(02)00036-2.

Gault, E.D., Horz, F., Brownlee, E.D., Hartung, B.J., 1974. Mixing of the lunar regolith. In: Proceedings of the 5th Lunar and Planetary Science Conference, pp. 2365–2386.

Gold, T., Bilson, E., Baron, R.L., 1976. Electrical properties of Apollo 17 rock and soil samples and a summary of the electrical properties of lunar material at 450 MHz frequency. In: Proceedings of the 7th Lunar and Planetary Science Conference, pp. 2593–2603.

Gustafson, J.O., Bell, J.F., Gaddis, L.R., Hawke, B.R., Giguere, T.A., 2012. Characterization of previously unidentified lunar pyroclastic deposits using lunar reconnaissance orbiter camera data. J. Geophys. Res., Planets 117 (E12). https://doi.org/10.1029/2011JE003893.

Haruyama, J., Ohtake, M., Matsunaga, T., Otake, H., Ishihara, Y., Masuda, K., Yokota, Y., Yamamoto, S., 2014. Data products of SELENE (Kaguya) terrain camera for future lunar missions. In: Proceedings of the 45th Lunar and Planetary Science Conference, p. 1777.

Hauri, E.H., Weinreich, T., Saal, A.E., Rutherford, M.J., Van Orman, J.A., 2011. High pre-eruptive water contents preserved in lunar melt inclusions. Science 333 (6039), 213–215. https://doi.org/10.1126/science.1204626.

Hawke, B.R., Coombs, C.R., Clark, B., 1990. Ilmenite-rich pyroclastic deposits: an ideal lunar resource. In: Proceedings of the 20th Lunar and Planetary Science Conference, pp. 249–258.

Hawke, B.R., Coombs, C.R., Gaddis, L.R., Lucey, P.G., Owensby, P.D., 1989. Remote sensing and geologic studies of localized dark mantle deposits on the moon. In: Proceedings of the 19th Lunar and Planetary Science Conference, pp. 255–268.

Hawke, B.R., Spudis, P.D., Clark, P.E., 1985. The origin of selected lunar geochemical anomalies: implications for early volcanism and the formation of light plains. Earth Moon Planets 32 (3), 257–273. https://doi.org/10.1007/BF00054216.

Head, J.W., 1974. Lunar dark-mantle deposits: possible clues to the distribution of early mare deposits. Geochim. Cosmochim. Acta 1, 207–222.

Head, J.W., Wilson, L., 1979. Alphonsus-type dark-halo craters: morphology, morphometry and eruption conditions. In: Proceedings of the 10th Lunar and Planetary Science Conference, pp. 2861–2897.

Head, J.W., Wilson, L., 2017. Generation, ascent and eruption of magma on the Moon: new insights into source depths, magma supply, intrusions and effusive/explosive eruptions (part 2: predicted emplacement processes and observations). Icarus 283, 176–223. https://doi.org/10.1016/j.icarus.2016.05.031.

Henriksen, M.R., Manheim, M.R., Burns, K.N., Seymour, P., Speyerer, E.J., Deran, A., Boyd, A.K., Howington-Kraus, E., Rosiek, M.R., Archinal, B.A., Robinson, M.S., 2017. Extracting accurate and precise topography from LROC narrow angle camera stereo observations. Icarus 283, 122–137. https://doi.org/10.1016/j.icarus.2016.05.012.

Houghton, B.F., Carey, R.J., 2015. Pyroclastic fall deposits. In: Sigurdsson, H., Houghton, B.F., McNutt, S.R., Rymer, H., Stix, J. (Eds.), The Encyclopedia of Volcanoes, 2nd ed. Academic Press, San Diego, pp. 599–616.

Houghton, B.F., Gonnermann, H.M., 2008. Basaltic explosive volcanism: constraints from deposits and models. Chem. Erde 68 (2), 117–140. https://doi.org/10.1016/j.chemer.2008.04.002.

Houghton, B.F., Wilson, C.J.N., Pyle, D.M., 2000. Pyroclastic fall deposits. In: Sigurdsson, H., Houghton, B.F., McNutt, S.R., Rymer, H., Stix, J. (Eds.), The Encyclopedia of Volcanoes. Academic Press, San Diego, pp. 555–569.

Jawin, E.R., Besse, S., Gaddis, L.R., Sunshine, J.M., Head, J.W., Mazrouei, S., 2015. Examining spectral variations in localized lunar dark mantle deposits. J. Geophys. Res., Planets 120 (7), 1310–1331. https://doi.org/10.1002/2014JE004759.

Jozwiak, L.M., Head, J.W., Wilson, L., 2015. Lunar floor-fractured craters as magmatic intrusions: geometry, modes of emplacement, associated tectonic and volcanic features, and implications for gravity anomalies. Icarus 248, 424–447. https://doi.org/10.1016/j.icarus.2014.10.052.

Kiefer, W.S., MacKe, R.J., Britt, D.T., Irving, A.J., Consolmagno, G.J., 2012. The density and porosity of lunar rocks. Geophys. Res. Lett. 39 (7), 1–5. https://doi.org/10.1029/2012GL051319.

Lucey, P.G., Taylor, G.J., Malaret, E., 1995. Abundance and distribution of iron on the Moon. Science 268 (5214), 1150–1153. https://doi.org/10.1126/science.268.5214.1150.

Nozette, S., 1995. The Clementine mission: past, present, and future. Acta Astronaut. 35 (Suppl. 1), S161–S169. https://doi.org/10.1016/0094-5765(94)00181-K.

Paige, D.A., Foote, M.C., Greenhagen, B.T., Schofield, J.T., Calcutt, S., Vasavada, A.R., Preston, D.J., Taylor, F.W., Allen, C.C., Snook, K.J., Jakosky, B.M., Murray, B.C., Soderblom, L.A., Jau, B., Loring, S., Bulharowski, J., Bowles, N.E., Thomas, I.R., Sullivan, M.T., Avis, C., De Jong, E.M., Hartford, W., McCleese, D.J., 2010. The lunar reconnaissance orbiter diviner lunar radiometer experiment. Space Sci. Rev. 150 (1–4), 125–160. https://doi.org/10.1007/s11214-009-9529-2.

Papike, J.J., 1998. Planetary materials. Rev. Miner. 36.

Pieters, C.M., Boardman, J., Buratti, B., Chatterjee, A., Clark, R., Glavich, T., Green, R., Head, J.W., Isaacson, P., Malaret, E., McCord, T.B., Mustard, J.F., Petro, N.E., Runyon, C., Staid, M.I., Sunshine, J.M., Taylor, L., Tompkins, S., Varanasi, P., White, M., 2009. The Moon mineralogy mapper (M3) on Chandrayaan-1. Curr. Sci. 96 (4), 500–505. https://doi.org/10.2307/24105459.

Pyle, D.M., 1989. The thickness, volume and grainsize of tephra fall deposits. Bull. Volcanol. 51, 1–15. https://doi.org/10.1007/BF01086757.

Robinson, M.S., Brylow, S.M., Tschimmel, M., Humm, D., Lawrence, S.J., Thomas, P.C., Denevi, B.W., Bowman-Cisneros, E., Zerr, J., Ravine, M.A., Caplinger, M.A., Ghaemi, F.T., Schaffner, J.A., Malin, M.C., Mahanti, P., Bartels, A., Anderson, J.A., Tran, T.N., Eliason, E.M., McEwen, A.S., Turtle, E., Jolliff, B.L., Hiesinger, H., 2010. Lunar reconnaissance orbiter camera (LROC) instrument overview. Space Sci. Rev. 150 (1), 81–124. https://doi.org/10.1007/s11214-010-9634-2.

Romero, J.E., Douillet, G.A., Vargas, S.V., Bustillos, J., Troncoso, L., Díaz Alvarado, J., Ramón, P., 2017. Dynamics and style transition of a moderate, vulcanian-driven eruption at tungurahua (Ecuador) in February 2014: pyroclastic deposits and hazard considerations. Solid Earth 8, 697–719. https://doi.org/10.5194/se-8-697-2017.

Sato, M., 1976. Oxygen fugacity and other thermochemical parameters of Apollo 17 high-Ti basalts and their implications on the reduction mechanism. In: Proceedings of the 7th Lunar and Planetary Science Conference, pp. 1323–1344.

Schmitt, H.H., Trask, N.J., Shoemaker, E.M., 1967. Geologic Map of the Copernicus Quadrangle of the Moon. USGS Misc. Invest. Map i-515, U.S. Geological Survey, Reston, Va.

Smith, D.E., Zuber, M.T., Jackson, G.B., Cavanaugh, J.F., Neumann, G.A., Riris, H., Sun, X., Zellar, R.S., Coltharp, C., Connelly, J., Katz, R.B., Kleyner, I., Liiva, P., Matuszeski, A., Mazarico, E.M., McGarry, J.F., Novo-Gradac, A.-M., Ott, M.N., Peters, C., et al., 2010. The lunar orbiter laser altimeter investigation on the lunar reconnaissance orbiter mission. Space Sci. Rev. 150 (1), 209–241. https://doi.org/10.1007/s11214-009-9512-y.

Taddeucci, J., Edmonds, M., Houghton, B.F., James, M.R., Vergniolle, S., 2015. Hawaiian and strombolian eruptions. In: Sigurdsson, H., Houghton, B.F., McNutt, S.R., Rymer, H., Stix, J. (Eds.), The Encyclopedia of Volcanoes, 2nd ed. Academic Press, San Diego, pp. 485–503.

Walker, G.P.L., 1973. Explosive volcanic eruptions - a new classification scheme. Geol. Rundsch. 62 (2), 431–446. https://doi.org/10.1007/BF01840108.

Wilhelms, D.E., McCauley, J.F., 1971. Geologic Map of the Near Side of the Moon. USGS Misc. Invest. Map i-703, U.S. Geological Survey, Reston, Va.

Wilson, L., Head, J.W., 2017. Generation, ascent and eruption of magma on the Moon: new insights into source depths, magma supply, intrusions and effusive/explosive eruptions (part 1: theory). Icarus 283, 146–175. https://doi.org/10.1016/j.icarus.2016.05.031.

Wieczorek, M.A., Neumann, G.A., Nimmo, F., Kiefer, W.S., Taylor, G.J., Melosh, H.J., Phillips, R.J., Solomon, S.C., Andrews-Hanna, J.C., Asmar, S.W., Konopliv, A.S., Lemoine, F.G., Smith, D.E., Watkins, M.M., Williams, J.G., Zuber, M.T., 2013. The crust of the Moon as seen by GRAIL. Science 339, 671–675. https://doi.org/10.1126/science.1231530.